Multi frame radiography of supersonic water jets interacting with a foil target

D. Maler ✉ ⓘ ; O. Belozerov ⓘ ; A. Godinger ⓘ ; S. Efimov ⓘ ; J. Strucka ⓘ ; Y. Yao; K. Mughal ⓘ ;
B. Lukic ⓘ ; A. Rack ⓘ ; S. N. Bland ⓘ ; Ya. E. Krasik ⓘ

Check for updates

View Online

Export Citation

Multi frame radiography of supersonic water jets interacting with a foil target

D. Maler,[1,a] ID O. Belozerov,[1] ID A. Godinger,[1] ID S. Efimov,[1] ID J. Strucka,[2] ID Y. Yao,[2] ID K. Mughal,[2] ID B. Lukic,[3] ID
A. Rack,[3] ID S. N. Bland,[2] ID and Ya. E. Krasik[1] ID

AFFILIATIONS

[1]Physics Department, Technion—Israeli Institute of Technology, Haifa 3200003, Israel
[2]Plasma Physics Group, Imperial College London, London SW7 2BW, United Kingdom
[3]European Synchrotron Radiation Facility, CS40220, 38043 Grenoble Cedex 9, France

[a]Author to whom correspondence should be addressed: daniel.maler@campus.technion.ac.il

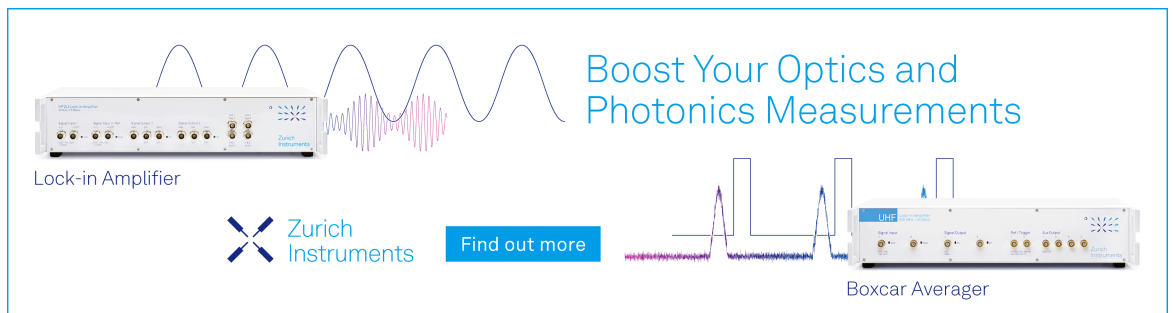## ABSTRACT

Pulsed-power-driven underwater electrical explosion of cylindrical or conical wire arrays produces supersonic water jets that emerge from a bath, propagating through the air above it. Interaction of these jets with solid targets may represent a new platform for attaining materials at high pressure ($>10^{10}$ Pa) conditions in a university-scale laboratory. However, measurements of the internal structure of such jets and how they interact with targets are difficult optically due to large densities and density contrasts involved. We utilized multi-frame x-ray radiographic imaging capabilities of the ID19 beamline at the European Synchrotron Radiation Facility to explore the water jet and its interaction with a 50 μm thick copper foil placed a few mm from the surface of water. The jet was generated with a ~130 kA-amplitude current pulse of ~450 ns rise time applied to a conical wire array. X-ray imaging revealed a droplet-type structure of the jet with an average density of <400 kg/m^3 propagating with a velocity of ~1400 m/s. Measurements of deformation and subsequent perforation of the target by the jet suggested pressures at the jet–target interface of ~5×10^9 Pa. The results were compared to hydrodynamic simulations for better understanding of the jet parameters and their interaction with the foil target. These results can be used in future research to optimize the platform, and extend it to larger jet velocities in the case of higher driving currents supplied to the wire array.

I. INTRODUCTION

The last decade has seen significant interest in the use of exploding wires/arrays of wires in liquids and solid dielectrics.[1,2] Research on exploding cylindrical wire arrays submerged in water has shown that extreme water parameters can be achieved on the implosion axis. This is due to the merging of shock waves from each individual wire's explosion and the subsequent convergence of this highly symmetric "merged" shock to the axis.[3] Experimental results and numerical simulations suggest that with ~0.5 MA driving current, the imploding convergent shock wave reaches pressures of ~3×10^{11} Pa and densities >2×10^3 kg/m^3 in the vicinity of the implosion axis in water.

Recently,[4–6] we demonstrated that placing a cylindrical wire array just below the surface of a water bath resulted in a jet propagating out of the water, into the air, along the axis of the array.

This behavior is due to the formation of "funnel-shaped" shock waves close to the top and bottom of the array, which redirect the flow of water behind the shock front into a jet. Utilizing conical arrays to maximize this effect resulted in the generation of supersonic, sub-millimeter diameter water jets, with velocities reaching up to ~4.5×10^3 m/s emerging from water. Experiments obtaining such jet velocities were driven by a pulsed-power generator that delivered a current pulse of ~0.4 MA in ~400 ns.[6] The shape and velocity of the jet depend on experimental parameters such as the geometry of the wire array and the thickness of the water layer above the array. Additionally, the energy-density deposition rate into the exploding wires, governed by the wire array and the pulsed-power generator, is a key parameter. In subsequent experiments,[7] we used shadowgraph imaging to study the collision of water jets with aluminum targets in the air, as well as the collision between two jets (also in the air), utilizing a smaller current drive

($\sim$300 kA, $\sim$1 μs rise time). Experimental results were compared with 2D hydrodynamic simulations coupled to the SESAME[8] Equations of State (EOS) for water, air, and aluminum. These suggested that even with relatively moderate drive currents / deposited energies, water pressures of $\sim 10^{10}$ Pa are attained at the collision point.

A natural extension to this research would be to scale these experiments to higher currents in the hope of attaining pressures $\geq 10^{11}$ Pa, the so-called high-energy density (HED) conditions, in the target or at the collision point between two or more jets. However, our experimental results to date have relied on shadowgraph and streak imaging techniques, which can obtain only the outline and the velocity of the jet. These measurements do not provide any meaningful insights into the internal structure of the jet as well as its interaction with a target. These properties of the jet need to be explored to validate our simulations and enable us to optimize the jet–target platform so that we can predict its scaling with current and achieve HED conditions on larger pulsed-power generators.

In this paper, we present the results of an investigation of the jet structure and the jet–target interaction performed at the micro-tomography beamline (ID19) of the European Synchrotron. ID19 provides a unique diagnostic tool for wire explosion studies, obtaining up to 256 frames of x-ray radiography at a photon average energy of $\sim$30 keV, with interframe separation of 176–704 ns, depending on the electron bunch structure employed. Each frame has high temporal ($\sim$60 ps)[9] and spatial (typically 32 μm) resolutions. Moreover, the beam is propagated over a distance ($\sim$8 m) sufficient for phase-contrast enhancement of material interfaces. This allows studies of shock wave dynamics even with small changes in density across its front.[10,11] Previously, ID19 has been

utilized to explore the internal structure of single exploding wires underwater,[12] the development of electro-thermal instabilities,[13] the dynamics of convergent shock waves produced by the explosion of cylindrical wire arrays, and the use of planar wire arrays for shock-induced hydrodynamic instability research in arbitrary geometries.[14,15]

This paper is structured as follows: in Sec. II, we describe the experimental setup and diagnostics used in the present research. In Sec. III, we present the experimental results that include electrical parameters of conical wire array explosion, jet velocity, and radiographs of the jet and its interaction with a thin copper target. In Sec. IV, we discuss the results of hydrodynamic simulations and compare them to the experiment. Finally, in Sec. V, we present our conclusions, which suggest that this method could be utilized to produce HED conditions in the targets with only university-scale pulsed-power facilities.

II. EXPERIMENTAL SETUP AND DIAGNOSTICS

In experiments, a compact pulsed-power generator was used, comprising one capacitor (Aerovox RTE model PX360E20, 100 kV, 1.38 μF, 50 nH) charged to 45 kV (stored energy of $\sim$1.4 kJ). This generator provides a current pulse of $\sim$130 kA in $\sim$450 ns to a conical wire array.

Figure 1 shows the experimental setup. The experimental chamber was mounted on top of the generator so that its windows were aligned with the synchrotron x-ray beam. During the experiments, the array was placed inside a Perspex capsule (65 mm in diameter) filled with de-ionized water. The capsule had two 100 μm thick glass windows at the point of entry and exit of the x-ray beam. In all experiments, the water level was set at
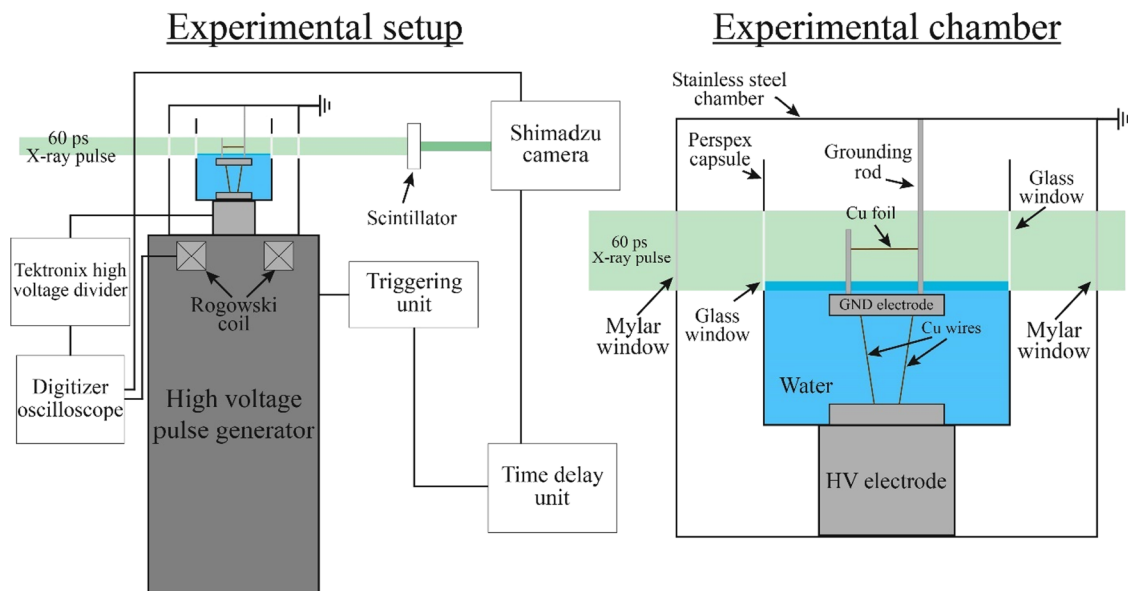

FIG. 1. Experimental setup.

~3–3.5 mm above the ground electrode. Electrical explosion of the conical array produced a supersonic jet propagating out of water. In some experiments, a $50 \, \mu m$ thick and $10 \times 50 \, mm^2$ copper foil target was placed ~7.5 mm above the water surface. In one experiment, the foil was inclined relative to the imaging system to be able to observe the emergence of the jet out of the foil's top surface [as can be seen in Figs. 4(a), 4(c), and 4(e)].

The conical array was 5 mm in diameter at the high voltage (HV) electrode and 10 mm in diameter at the ground (GND) electrode (apex angle −3.57°) as shown in Fig. 1. The array consisted of 20 copper wires equally distributed along the cone, each 30 mm in length and $90 \, \mu m$ in diameter. The length and diameter of the wires were chosen to achieve an almost critically damped discharge. Previously, the production of a critically damped discharge has been shown to produce the maximum energy deposition and rate of energy density deposition into the wires, and consequently, the strongest shock waves in water.[16]

Current (I) and voltage (V) measurements were performed using a self-integrated Rogowski coil and a P6015A Tektronix voltage divider, respectively, with the waveforms acquired using a Lecroy WaveRunner 8404M digitizing oscilloscope.

During the experiments, the synchrotron operated in four-bunch mode, providing a single pulse of almost collimated x rays every 704 ns. X rays were produced by two U32 undulators and filtered by diamond and beryllium windows in the x-ray beam path. The resulting spectrum was a broad undulator spectrum with harmonics spanning photon energies in the 15–50 keV range.[9,17] The x-ray pulses passed through the chamber, just above the conical wire array, and impinged on a $500 \, \mu m$ thick LYSO:Ce (Hilger Crystals, UK) scintillator which converted the x-ray beam to optical light. The x-ray beam provided illumination over a rectangular area of $12.8 \times 8 \, mm^2$ of the scintillator, whose optical emission was relayed via a pellicle beam splitter and Hasselblad lenses (magnification of 1) to a high-speed Shimadzu HPVX2 framing camera. The camera was positioned off-axis of the x-ray beam to prevent any heat/x-ray damage. This is not shown in Fig. 1 which presents a simplified diagram of the experimental setup. This imaging setup enabled us to track the dynamics of the jet and the target over a long time period (~5 μs before the jet leaves the field-of-view);

although this did limit resolution on the images to $32 \, \mu m$ to maintain a sufficiently large field-of-view. The decay time of the scintillator was ~30 ns; so there was no imprint of previous images on subsequent frames.

III. EXPERIMENTAL RESULTS

A. Typical discharge parameters and water jet structure

Figure 2(a) shows typical current (black line) and resistive voltage (red line) waveforms measured during a discharge of the generator into the conical wire array. The discharge current reached its maximum value of ~130 kA with a rise time of ~450 ns. Due to the large mass of wires, the wire array stays almost stationary during the period of energy deposition (while the current is non-zero) and any change in its inductance is negligibly small. Thus, we can calculate the resistive voltage across the wires from the measured voltage V as $V_{Res} = V - L_{load} \frac{dI}{dt}$, where $L_{load} = 22$ nH is the self-inductance of the wire array. This estimate agrees with the current and voltage measurements early in time, when the resistive voltage is negligible, and the voltage is given by $V = L_{load} \frac{dI}{dt}$.

In Fig. 2(b), we present the time evolution of power deposited into the wire array, calculated as $P(t) = I(t) \cdot V_{res}(t)$ (black line), in addition to the cumulative deposited energy (red line). In total, 78% of the electrical energy stored in the capacitor at the beginning of the discharge was transferred into the wires by the end of the current pulse, with ~50% energy being rapidly deposited over a period of only ~200 ns. The total specific energy deposition into the wire was estimated at ~32 kJ/g (corresponding to ~21 eV/ atom).

As the array explodes, the imploding conical shock wave converged symmetrically along the axis of the array, producing high pressure and density in the shocked region and leading to the generation of a high velocity water jet propagating toward the air–water interface.[5,6]

Figure 3 shows radiography images of the internal structure of the jet launched out of the water and propagating in the air. Figure 3(a) shows a background image where the jet has not yet
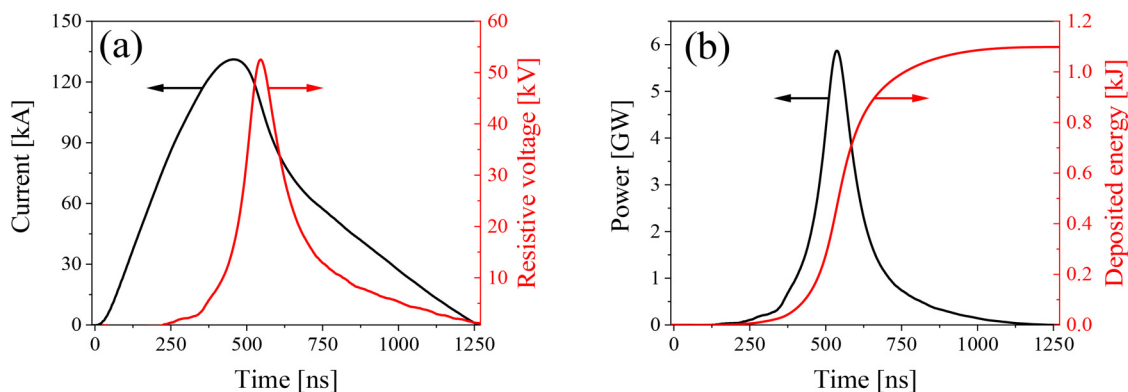
FIG. 2. Waveforms of the current and resistive voltage in (a) and power and deposited energy in (b).
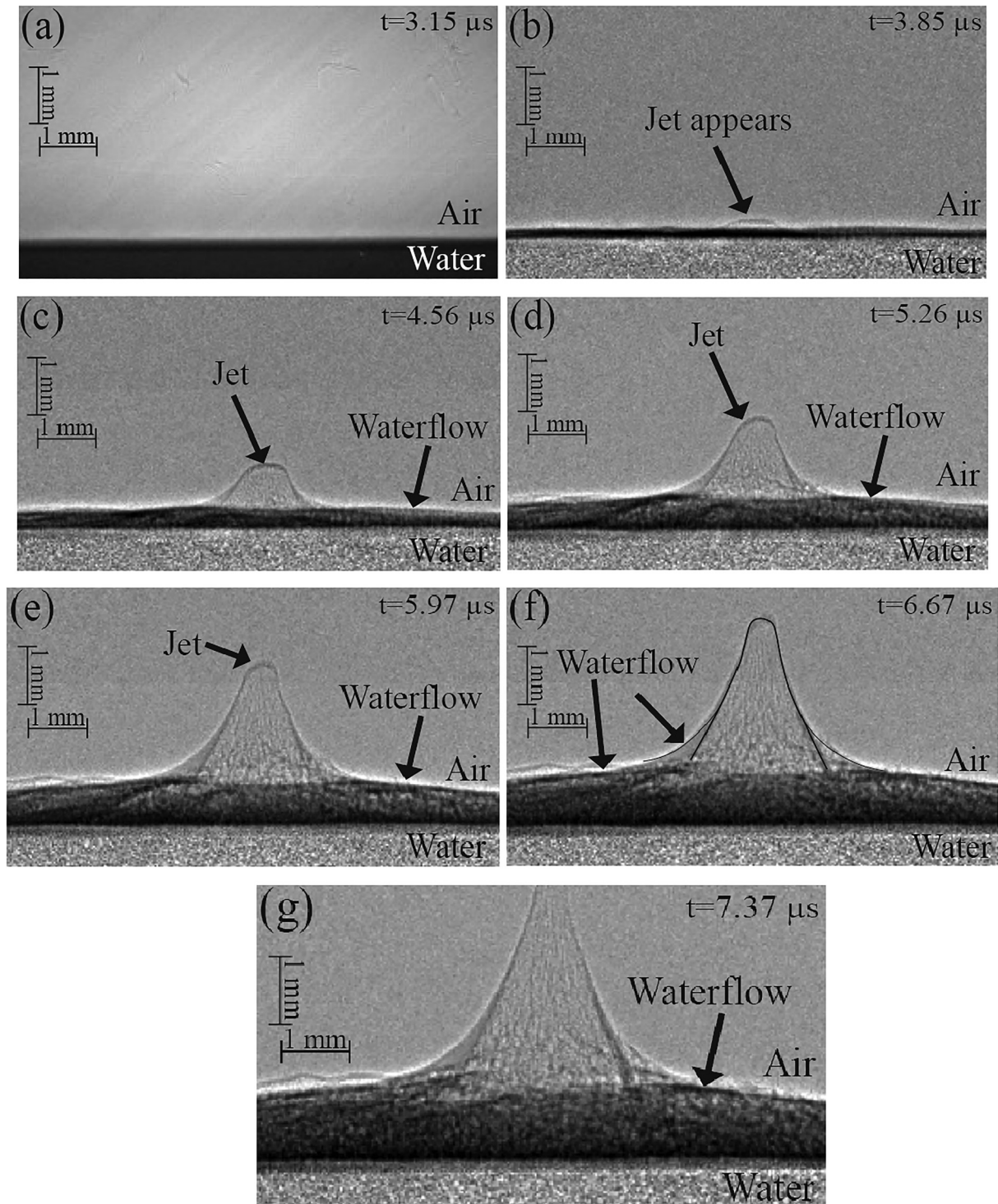
FIG. 3. Radiography of the water jet propagating in air. The time origin corresponds to the beginning of the current discharge. In image (f), the contour of the jet and the surrounding waterflow are emphasized by black lines. Image (a) is taken as the background image which is subtracted from images (b)–(g) to enhance the jet structure and features.

emerged from the water, showing the initial water level. Figure 3(b) depicts the beginning of the jetting process launched from water. As the jet propagates, the diameter of its tip (the "head" of the jet) decreases [see Figs. 3(c)–3(g)]. This could be related to non-uniform axial velocity distribution having larger velocities in the "head." Radiography shows that the internal structure of the jet consists of elongated drop-like structures directed along its propagation direction. At the tip of the jet, the Weber number is approximately $We \sim 10^7$, suggesting that inertial effects strongly dominate surface tension. The outline of the jet is clearly visible throughout the measurement due to phase-contrast edge-enhancement producing a clear boundary between the water and the air. At the base of the jet, a water interface connecting the jet to the waterflow is visible, marked as "waterflow" in Fig. 3(f). This interface is likely caused by inertial effects and not viscosity, as the Reynolds number of the jet is $Re \sim 10^5$.

Using the radiographs in Fig. 3, the tip of the jet was calculated to travel with an average velocity of 1200 ± 90 m/s, without a significant decrease in velocity throughout the measurement. This value is profoundly slower than the values reported in earlier research[6] where the jet reached velocity up to $\sim 4.5 \times 10^3$ m/s. This difference in jet velocities is related to a thicker (~ 3–3.5 mm) water layer above the array, which substantially decreased the velocity of the jet as it emerged from the water obtained in earlier research on MAGEN generator.[5] Additionally, the present experiments utilized an exploding wire array that covered only $\sim 11.5\%$ of the conical area, calculated as $N\varnothing_{wire}/\pi\varnothing_{cone}$, where N is the number of wires around the circumference of the cone, $\varnothing_{wire}$ is the diameter of the wires, and $\varnothing_{cone}$ is the diameter of the cone at the high voltage electrode. In comparison, the conical wire array utilized in the MAGEN experiments covered $\sim 29\%$ of the conical area. Due to the same energy density and the energy-density deposition rate produced by electrical discharges, it is reasonable to assume that the wires in both these experiments exploded at approximately the same pressure.[18] Consequently, the pressure on the axis produced by this explosion is likely to be significantly lower for the experiments presented here. Wire explosion leads to fast radial expansion of the wire and generation of cylindrically diverging strong shock waves. The shock wave intensity decreases as $P(r) = P_{in}\left(\frac{r_w}{r}\right)^{0.7}$, where $P(r)$ is the pressure behind the shock wave front, r is the distance from the exploding wire, r_w is the wire radius, and P_{in} is the initial pressure of the shock wave at its origin. The initial pressure P_{in} is defined at the surface of the exploding wire positioned at r_w.[19] The overlap of individual diverging shocks leads to the formation of a symmetric converging shock.[20] The distance, with respect to the initial position of the wires, where this symmetric shock is formed, depends on the inter-wire distance. Namely, for smaller inter-wire spacing, the radial distance where one obtains the formation of symmetrical converging shock is smaller. Thus, in the case of the MAGEN generator, the converging shock forms closer to the exploding wires with higher pressure when compared to the presented experiments. This leads to higher pressure in the vicinity of the shock implosion and, respectively, to higher jet velocity.

Simple considerations of the x-ray attenuation in Fig. 3, which assumed an average beam energy between 20 and 30 keV, suggest that the average mass density inside of the jet was <800 kg/m³. Estimates utilizing the full undulator spectrum of the source

(calculated in Oasys[21]) suggest a lower density, with an upper bound of 400 kg/m³ at $t = 6.67\,\mu$s. These estimates further suggest that the jet structure cannot be considered as a uniform medium. At present, we do not know the details of this structure and we can only consider that the jet may contain bubbles of saturated vapor, tensed water molecules, or voids.

B. Impact of the water jet on a copper foil

In a separate set of experiments, a $50\,\mu$m thick copper foil was placed ~ 10.5 mm above the ground electrode. The aim of this experiment was to observe the impact of the jet on this foil and the following dynamics.

Figures 4(a), 4(c), and 4(e) show radiographic images obtained when the foil was inclined relative to the jet (and the line-of-sight) to enable stereoscopic imaging of the collision dynamics. In these experiments, the water height above the ground electrode was reduced to slightly below ~ 3–3.5 mm, moderately increasing the speed of the jet to 1400 ± 90 m/s. As a result of the jet impact, the copper foil was observed to stretch with approximately radially symmetric material flow. This suggests the exertion of high pressure on the target, leading to a high strain rate of the material. Shortly after, the foil is perforated by the jet with copper micro-particles seen propagating above the foil with the velocity of the waterflow. Assuming a cylindrical coordinate system, we measured the velocity of the copper micro-particles projected on the r–z plane. Particles with a characteristic size of $\sim 150\,\mu$m propagated with velocities of 700 ± 100 m/s axially upward.

Additionally, the strain rate $\dot\gamma$ in the stretched copper foil was estimated using the full set of ~ 25 measured x-ray radiographs (704 ns interframe time) that show foil perforation. The images shown in Fig. 4 were selected from these to highlight qualitative dynamics of the jet-foil interaction. In the first $\sim 2.1\,\mu$s after the jet perforates the foil, a bulge appears with an initial strain rate of $\dot\gamma = 8 \times 10^5$ s^{-1}. This value decreases to $\sim 2 \times 10^5$ s^{-1} within several μs of the jet impact as the foil stretches further. Moreover, after the impact with the jet and subsequent foil perforation, a bulge appears in the copper foil, which expands with an average velocity of ~ 180 m/s. This velocity corresponds to the obtained strain rate of 8×10^5 s^{-1} multiplied by the characteristic size of the bulge of 2.24×10^{-2} cm [see Fig. 4(b)].

IV. DISCUSSION

X-ray radiography images presented in Fig. 3 showed an internal jet structure that significantly differs from water at ambient conditions. These images suggest that the jet contains water droplets with a typical size of $\sim 60\,\mu$m, which are elongated in the direction of jet propagation. It is understood that radiography is integrated along the line-of-sight through ~ 1 mm diameter jet. Considering that the droplets are randomly distributed inside the jet, several of the droplets could be seen in each radiograph. Figure 5 shows a magnified view of the relevant part of Fig. 3(e) where these elongated structures are clearly seen.

At present, we do not have a conclusive explanation for this droplet structure. There are three possible phenomena that could be responsible for this structure. First, numerical simulations performed in our previous research[6] indicated that axial velocity
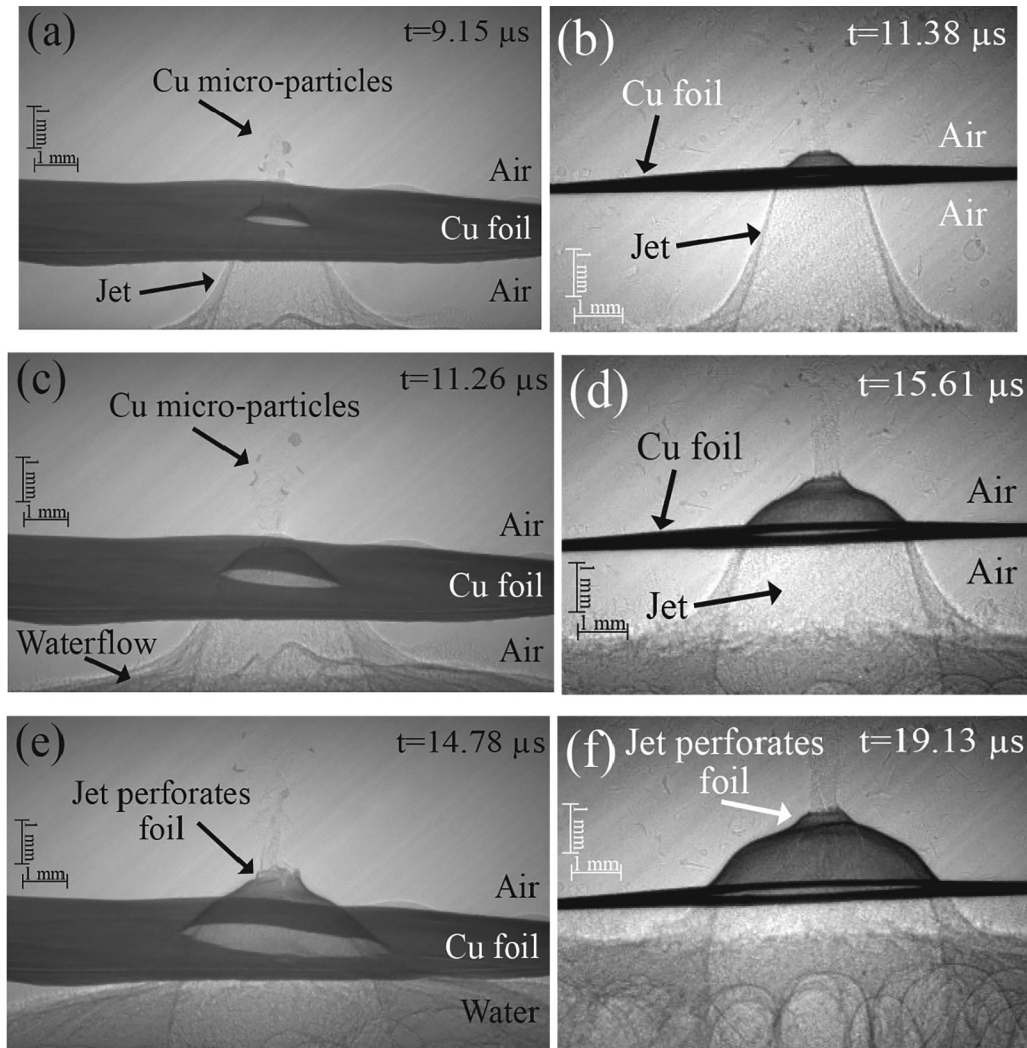
FIG. 4. Radiography of the water jet impacting upon a 50 μm thick copper foil target. Time origin corresponds to the beginning of the discharge current. Intensities of (b), (d), and (f) were enhanced to better present qualitative features of the jet perforating the foil.

distribution (along the propagation direction of the jet) within the jet is non-uniform, with a maximal velocity at the jet tip. However, these simulations did not account for the emergence of the jet into air. Nevertheless, if this velocity distribution persisted in the air, it could lead to stretching of the jet. Another potential explanation for the structure is due to air–water mixing. Research of water jets used for surface cleaning showed that the structure of fast propagating water jets (velocities up to ~800 m/s) in the air is characterized by droplet structure.[22,23] Here, the air surrounding the jet is entrained into the waterflow, creating a mixed layer of air and water drops due to fast growing Kelvin–Helmholtz instability. Finally, we cannot exclude cavity formation due to the interaction of multiple rarefaction waves, which could be formed by re-loading at the jet/air interface, as the reason for the droplet structure. It is

understood that additional research on jet emergence and propagation in air is still required.

The x-ray radiographs presented in this work could not be used to obtain an accurate mass density of the jet due to the low x-ray attenuation of a ~20 keV beam passing through ~1 mm of water. However, it was possible to set an upper estimate on the density of the jet of ≤400 kg/m^3.

A. Analytical consideration of the jet impact using conservation laws and the Tait EOS

As the jet impacts the copper foil, a shock is transmitted into copper, and due to the acoustic impedance mismatch, a second shock is reflected into the jet. A similar situation was considered in
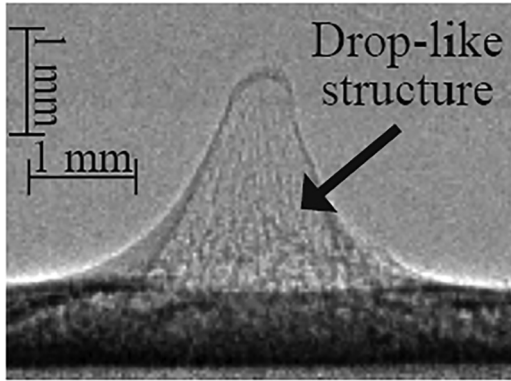
FIG. 5. Enhanced view of Fig. 3(e) showing the internal drop-like structure of the jet.

earlier research,[24] where the interaction of a shock propagating in water and impacting a copper target was analyzed using the equations for conservation of mass and momentum,

$$u_w + D_w = \sqrt{\frac{P_w - P_{jet}}{\rho_w(\rho_w/\rho_{jet} - 1)}}, \qquad (1)$$

$$u_{jet} - u_w = \sqrt{\frac{(P_w - P_{jet})(\delta_w - \delta_{jet})}{\rho_0 \delta_{jet} \delta_w}}, \qquad (2)$$

$$D_{Cu} = \sqrt{\frac{(P_{Cu} - P_0)\delta_{Cu}}{\rho_0(\delta_{Cu} - 1)}}, \qquad (3)$$

$$u_{Cu} = \sqrt{\frac{(P_{Cu} - P_0)(\delta_{Cu} - 1)}{\rho_0 \delta_{Cu}}}, \qquad (4)$$

$$P_{Cu} = P_w, \qquad (5)$$

$$u_{Cu} = u_w. \qquad (6)$$

Here, D_w is the velocity of the reflected shock wave in water, P_w and P_{Cu} are the pressures at the water–copper interface, D_{Cu} is the velocity of the shock wave in the copper foil, $\delta_{Cu} = \rho_{Cu}/\rho_{Cu0}$ is the compression of the copper foil, δ_w is the compression of water, and u_{jet}, P_{jet}, and ρ_{jet} are the jet velocity, pressure, and density, respectively. For simplicity, the pressure and density in the jet were taken to be at ambient conditions. u_{Cu} and u_w are copper and water material velocities at the water–copper target interface. Using this approach, we can describe the transmitted shock wave and the reflected shock wave in the jet by the same equations for conservation of mass and momentum across each of the shocks in combination with the isothermal Tait[25] EOS, given by $P \approx A \cdot (\delta^n - 1)$. Here, P is the pressure, n is the adiabatic index, A

is a material-dependent constant, and $\delta = \rho/\rho_0$ is the compression ratio, where ρ_0 and ρ are the ambient and shock-compressed mass density, respectively. The Tait EOS is known to be valid in shock-compressed water for pressure $\leq 5 \times 10^9$ Pa.[26] Equations (1)–(6) were solved, coupled to the Tait EOS, to obtain the pressure and density in water and copper, at the water–copper interface. For water, $A = 3 \times 10^8$ Pa and $n = 7.15$, while for copper, $A = 2.5 \times 10^{10}$ Pa and $n = 4$.[27] The solution yielded copper pressure and density of $\sim 4.7 \times 10^9$ Pa and $\sim 9.2 \times 10^3$ kg/m^3. The water density at the water–copper interface is $\sim 1.48 \times 10^3$ kg/m^3.

B. 1D and 2D hydrodynamic simulations of the jet impact

To obtain a more detailed model of material behavior leading to the perforation of the copper foil, we performed a numerical simulation of the process. Initially, we utilized an in-house 1D hydrodynamics code[28] to solve Euler's equations in Lagrange coordinates and over consecutive time steps. These equations are derived from the conservation of mass, momentum, and energy, and are given by

$$\frac{\partial(r^2)}{\partial s} = \frac{2}{\rho}, \qquad (7)$$

$$\frac{\partial v}{\partial t} = -r\frac{\partial p}{\partial s}, \qquad (8)$$

$$\frac{\partial \varepsilon}{\partial t} = -p\frac{\partial}{\partial t}\left(\frac{1}{\rho}\right), \qquad (9)$$

where ρ is the mass density, t is the temperature, p is the pressure, ε is the internal specific energy, and v is the radial velocity of the material. The Lagrange coordinate s is defined as $s = \int_0^r \rho(y, t)y\,dy$. Equations (7)–(9) are solved with the material closure given by the SESAME EOS tables[8] for water, copper, and air so that the pressure $P = P(\rho, \varepsilon)$ and temperature $T = T(\rho, \varepsilon)$ can be related to the mass density and internal specific energy of the materials. In the simulation, the radial coordinates were divided into cells, each containing a single material (either water, copper, or air). The simulation was performed in a 1D cylindrical coordinate system, which can be considered as close to the Cartesian system for large radii and small distances between the jet and the target. The resulting simulation can reproduce the experimental conditions—a high-speed water jet impacting a copper target—at large radii from the origin. The simulation was initiated with the cells corresponding to the copper foil located at a radial distance of 20 mm from the origin. The cells adjacent to the 50 μm thick copper foil were initiated as water cells at ambient density and with a radial velocity of 1.4×10^3 m/s aimed toward the copper foil, approximating the conditions present in the experiment prior to the jet impact. The 1D simulation scheme is presented in Fig. 6.

The ambient water density was chosen for simplicity, allowing the application of the water EOS outside of the negative pressure region, where the used SESAME EOS tables struggle to predict correct material behavior. The results of these simulations showed

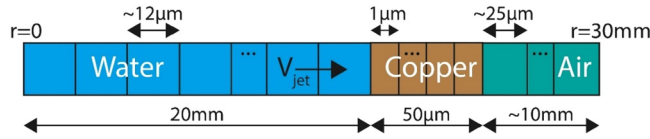<div style="writing-mode: vertical-lr">17 April 2024 11:07:44</div>

FIG. 6. 1D simulation scheme. $r = 0$ notes the axis origin.

that the pressure reaches $\sim 5 \times 10^9$ Pa at the water–copper interface, with water and copper densities reaching up to $\sim 1.45 \times 10^3$ and $\sim 9.2 \times 10^3$ kg/m^3, respectively. These results agree with the analytical estimates obtained in Sec. IV A which were performed with a simple Tait EOS.

Importantly, the above estimates of the water and copper parameters were obtained by methods that did not account for effects due to additional dimensions. To account for these effects, we also performed simulations with an in-house two-dimensional (2D) hydrodynamics code.[7,14] In this simulation, we solved the 2D Euler's equations in a Lagrangian form given by

$$\frac{\partial \rho}{\partial t} + \vec{\nabla} \cdot (\rho \vec{v}) = 0, \tag{10}$$

$$\frac{\partial \rho \vec{v}}{\partial t} + \vec{\nabla}(\rho \vec{v} \cdot \vec{v}) + \vec{\nabla} P = 0, \tag{11}$$

$$\frac{\partial \rho \varepsilon}{\partial t} + \vec{\nabla} \cdot [(\rho \varepsilon + P) \vec{v}] = 0, \tag{12}$$

where ρ, ε, $\vec{v}$, and P are the density, internal energy, velocity, and pressure, respectively. Equations (10)–(12) were coupled to the SESAME EOS tables.[8] In the simulation, the space was divided into a triangular mesh with a characteristic triangle size of $\sim 2\,\mu$m, and each triangle was assigned a single material. During the simulation, the vertices of each triangle were moved according to the sum of the forces acting on them, changing their total area. Once the mesh was evolved, the mass density and internal energy were calculated for each mesh element, enabling the estimation of pressure and temperature according to the SESAME EOS.

In this simulation, we did not aim to simulate the production of the jet, as this was considered in earlier research.[6] Instead, we initiated the simulation with a fully formed water jet placed against a $50\,\mu$m thick copper foil. The initial velocity of the water elements was set to 1.4×10^3 m/s. As in the 1D simulation, for simplicity, the mass density of the jet was set to ambient water density. However, the Lagrangian mesh used in these simulations could not replicate the perforation phenomena visible in the experiment. Due to this discrepancy, the simulation was only used to estimate the copper and water material properties for the first ~ 20 ns after the jet impact. The parameters obtained in the 2D simulation suggested that at the water–copper interface, the pressure reaches $\sim 5.5 \times 10^9$ Pa and densities reach $\sim 1.45 \times 10^3$ and $\sim 9.3 \times 10^3$ kg/m^3 for water and copper, respectively. These results showed slightly larger values of pressure and density of copper than those obtained by analytical modeling or 1D simulations. However, it is understood that for a lower jet density
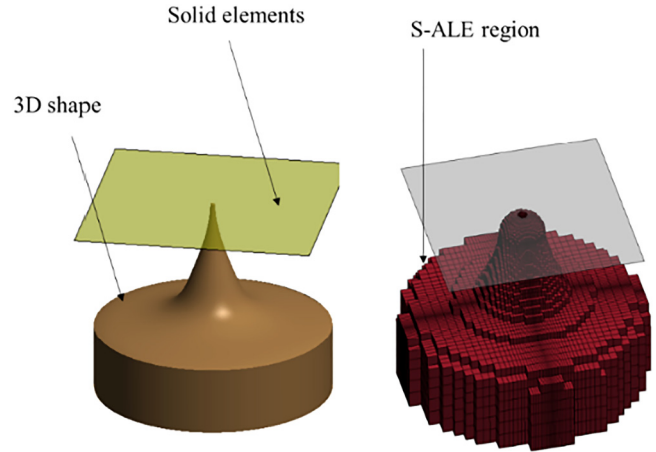

FIG. 7. Schematic representation of the simulation geometry (left) and S-ALE cells (right).

at impact (lower than ambient density), these parameters will be smaller up to a factor of 2.5.

Currently, the data obtained do not allow us to make a firm statement regarding the internal structure of the water jet. It is unclear if the jet consists of droplets at ambient density with surrounding voids, or if it should be treated as a uniform body at sub-ambient density. Nevertheless, the small initial contact area of the jet observed in the experiments suggests that the pressure exerted by a jet made of droplets at ambient density should be comparable to that of a uniform jet at ambient density. This is true on a time-scale of at least ~ 130 ns—the time it would take a rarefaction wave to reverberate along the length of a $100\,\mu$m droplet at the tip of the jet and for off-loading to begin. The precise pressure may lie in between the two extremes, namely, the pressure exerted on the foil by a jet of ambient density water and the pressure of a jet of reduced density. It is understood that this issue requires further investigation at facilities with significantly greater magnification where the internal structure of the jet can be probed quantitatively. Finally, we note that the subsequent dynamics of the foil impacted by the jet are reasonably matched by 3D simulation with a uniform ambient density jet, as will be further discussed in Sec. IV C.

As a comparison, in previous research,[6] we obtained supersonic jets with velocities up to $\sim 4.5 \times 10^3$ m/s. If we replicate the above simulations, again assuming ambient water in the jet moving at 5×10^3 m/s, upon the impact with the copper target, the pressure at the water–target interface reaches $\sim 3.5 \times 10^{10}$ Pa and mass densities of ~ 1.94 kg/m^3 and $\sim 11.1 \times 10^3$ kg/m^3 for water and copper, respectively. These properties are nearing the high-energy-density regime which is often defined as pressures $\geq 10^{11}$ Pa.

C. 3D hydrodynamic simulations of jet interaction and foil perforation

Finally, we performed a full 3D simulation using a commercial code to investigate the jet impact and its interaction with the

TABLE I. Copper material parameters for elastic–plastic behavior.[33]

Mass density	ρ (kg/m³)	8930
Shear modulus	G (Pa)	4.77×10^{10}
Hardening modulus	Eh (Pa)	3×10^{9}
Yield stress	σ_y (Pa)	3×10^{8}
Maximum principle strain	ε_{pmax}	0.5

TABLE II. Mie–Grüneisen coefficients.

Description	Symbol	Copper[33]	Water[34]
Mass density	ρ (kg/m³)	8930	1000
Sound velocity	C (m/s)	3940	1490
Mie–Grüneisen coefficient	S_1	1.489	1.79
Mie–Grüneisen coefficient	S_2	0	0
Mie–Grüneisen coefficient	S_3	0	0
Mie–Grüneisen coefficient	Γ	2.02	1.65
Volume correction coefficient	A	0.47	…

copper foil in detail, including foil perforation and consequent formation of micro-particles. The aim of this simulation was to obtain the development of pressure distribution throughout the impacted copper foil during the first tens of nanoseconds after the jet impact.

These simulations were carried out using a commercial numerical solver LSDYNA[®29] utilizing the coupled Eulerian–Lagrangian method with a Structured Arbitrary Lagrangian–Eulerian (S-ALE) solver and an explicit solver. The simulation performs a full 3D, nonlinear, transient analysis of the system that includes large plastic deformations, shock wave behavior, and material behavior through the utilization of an EOS.

The water cells in this simulation were described by ALE cells, while the copper foil was modeled by hexahedral elements with eight nodes using an explicitly formulated reduced-integration scheme. The interaction between the fluid flow (water) and the solid deformable structure (copper) was calculated by the LSDYNA coupling algorithm. Performing the simulation in this way allows the fluid to move within the S-ALE elements following fluid equations, while also allowing the solid to be accurately modeled by structural equations throughout its hexahedral elements.
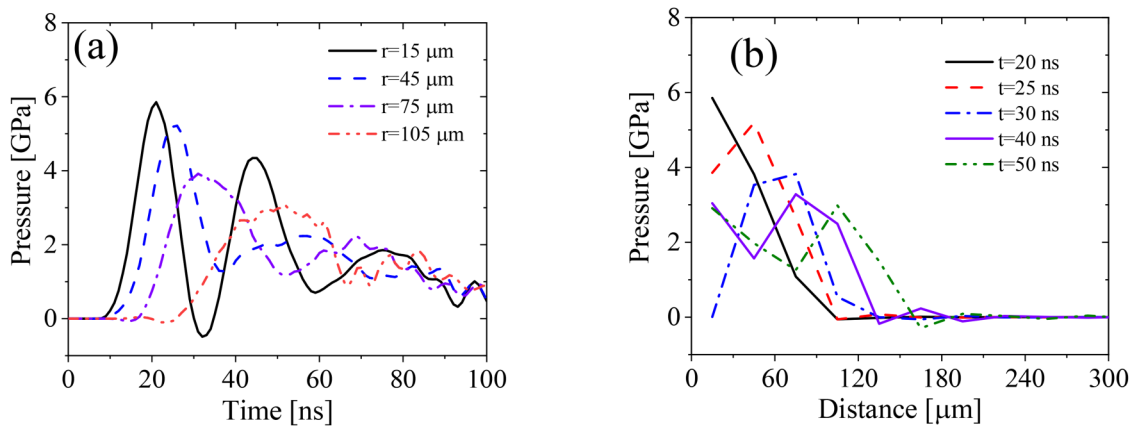

FIG. 8. Temporal pressure evolution in different radii from the point of impact (a) and radial pressure distribution in the foil for different times (b) for a 50-μm thick copper foil and jet velocity of 1.4×10^3.
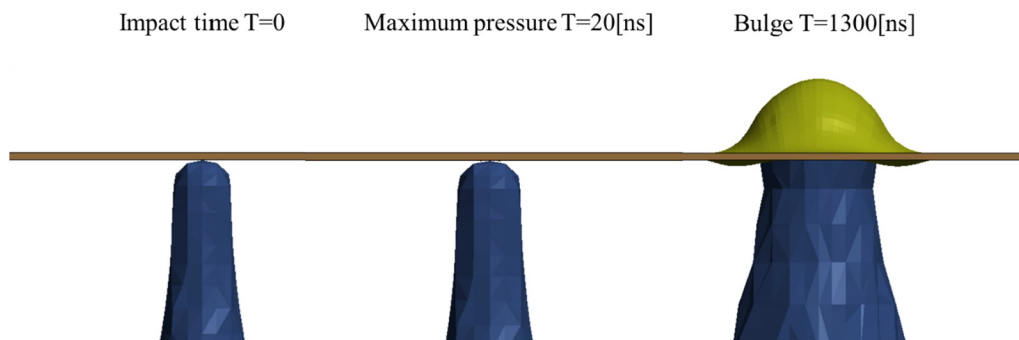

FIG. 9. Copper foil temporal deformation evolution for jet velocity of 1.4×10^3 m/s.
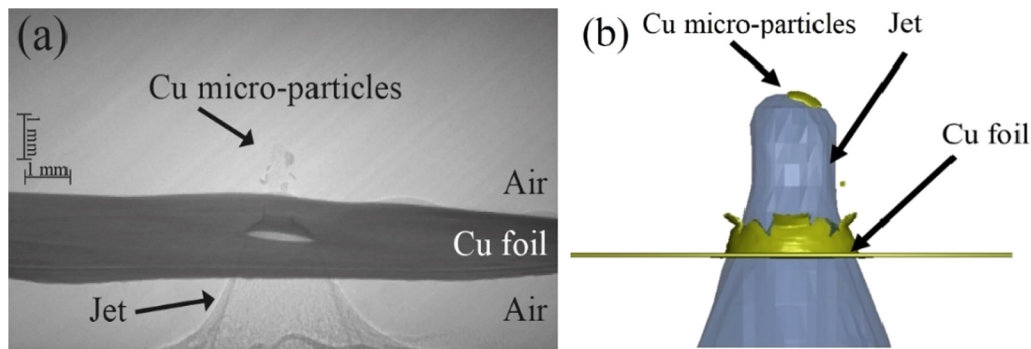
17 April 2024 11:07:44

FIG. 10. Fragmentation of the copper foil, in x-ray radiography image (a) (see Fig. 4) and as obtained in the numerical simulation (b).

In these simulations, the jet speed was set as an initial condition and the production of the shock wave from the explosion of the conical wire array was not simulated. At the beginning of the simulation, the water jet was considered to have a constant uniform velocity while the copper foil was stationary and un-constrained. Figure 7 shows the geometry of the jet utilized in the simulation, which was produced by revolving the outer contour of the water jet, obtained from the experimental x-ray radiographs, around its axis. The initial mass density and velocity of the jet were set to be 10^3 kg/m^3 and 1.4×10^3 m/s, respectively.

The copper foil was modeled by a simple elastic–plastic material model with kinematic[30] hardening (see Table I) in addition to a Mie–Grüneisen EOS[31,32] with its coefficients shown in Table II. These models by themselves do not include fragmentation or strain rate effects; therefore, we applied a simple maximum strain (ε_{pmax}) to the failure threshold. When the strain in a cell reaches this threshold, the element is deleted from the calculation. The water properties were modeled by a Mie–Grüneisen EOS shown in Table II.

Results from the simulation are shown in Fig. 8. Specifically, Fig. 8(a) shows the temporal evolution of pressure at a fixed radial distance from the jet impact point. This pressure is estimated as the average pressure of four adjacent copper cells that are, on average, at a radial distance r from the impact point of the jet. The maximum pressure reached in the simulations was 5.8×10^9 Pa in the vicinity of the impact point. At later times, the pressure close to the contact point ($r = 15\,\mu$m) oscillated with a period of $\sim$20 ns, corresponding to the acoustic time required for a sound wave to transit the thickness of the copper foil. The oscillations correspond to pressure waves induced by the transmitted shock as well as rarefaction waves from the free boundary of the foil. Interestingly, at the time of peak pressure at a radial distance of $15\,\mu$m, the average pressure at a radial distance of $105\,\mu$m was slightly negative, likely due to the stretching of the foil by its adjacent cells.

Figure 8(b) depicts the radial pressure distribution at five different times after the jet impact. The simulated results suggest that the maximum pressure of 5.8×10^9 Pa is obtained for $\sim$20 ns. This pressure drops sharply over $\sim$90 μm, corresponding to the physical size of the jet tip, meaning that the jet–target interaction can be considered spatially and temporally localized in the impacted zone.

Other effects, such as the deformation of copper to form a bulge (see Fig. 9), develop only later in time after approximately $\sim$1.3 μs. In comparison, shortly after the impact, the foil starts to fragment. The velocity of the fragments predicted by the simulation is $\sim$800 m/s, in agreement with the experimental observation presented in Sec. III B. Figure 10 shows that these fragments propagate above the jet which perforates the target.

V. SUMMARY

In the present work, we used multi-frame x-ray radiography to study the internal structure of a supersonic water jet produced using an electrically driven shaped charge, and its interaction with a stationary copper foil target. The x-ray images showed a well-defined outline of the water jet propagating in the air, as well as its internal structure consisting of clusters/drops elongated along the direction of propagation. These results imply a complex structure of the jet owing to water having a non-uniform axial velocity distribution as well as a complex interaction of shock waves and rarefaction waves within the water. The interaction of the jet with a thin metal foil produced a perforation in the foil due to the high pressure exerted on the material. Complementary 1D, 2D, and 3D numerical simulations of the experiment showed that a rapid and localized pressure pulse at the point of impact compressed the foil to a pressure of $\sim$6 $\times 10^9$ Pa. Additionally, the numerical simulations suggest that for a jet velocity of $\sim$5 $\times 10^3$ m/s, these pressures can reach values of 3.5×10^{10} Pa. Jet speeds of similar magnitude were reached in previous experiments that utilized larger pulsed-power generators. These results suggest the possibility of utilizing water jets, generated by underwater electrical explosion, as an attractive approach for studying matter in extreme conditions. Finally, additional research is required to understand the dynamics leading to the development of the water jet propagating in air; in particular, the reason for the development of its complicated internal structure.

ACKNOWLEDGMENTS

AUTHOR DECLARATIONS

Conflict of Interest

The authors have no conflicts to disclose.

Author Contributions

D. Maler: Conceptualization (equal); Data curation (equal); Formal analysis (equal); Investigation (equal); Methodology (equal); Software (equal); Writing – original draft (equal); Writing – review & editing (equal). **O. Belozerov:** Data curation (equal); Investigation (equal); Methodology (equal). **A. Godinger:** Methodology (equal); Software (equal); Writing – original draft (equal); Writing – review & editing (equal). **S. Efimov:** Data curation (equal); Investigation (equal); Methodology (equal); Supervision (equal). **J. Strucka:** Data curation (equal); Formal analysis (equal); Investigation (equal); Writing – original draft (equal); Writing – review & editing (equal). **Y. Yao:** Data curation (equal); Investigation (equal); Methodology (equal). **K. Mughal:** Data curation (equal); Investigation (equal); Methodology (equal). **B. Lukic:** Conceptualization (equal); Data curation (equal); Funding acquisition (equal); Investigation (equal); Project administration (equal); Resources (equal); Supervision (equal). **A. Rack:** Conceptualization (equal); Funding acquisition (equal); Project administration (equal); Supervision (equal); Writing – original draft (equal). **S. N. Bland:** Conceptualization (equal); Data curation (equal); Funding acquisition (equal); Investigation (equal); Project administration (equal); Supervision (equal); Writing – original draft (equal); Writing – review & editing (equal). **Ya. E. Krasik:** Conceptualization (equal); Data curation (equal); Formal analysis (equal); Funding acquisition (equal); Investigation (equal); Project administration (equal); Resources (equal); Supervision (equal); Writing – original draft (equal); Writing – review & editing (equal).

DATA AVAILABILITY

The data that support the findings of this study are available from the corresponding author upon request.

REFERENCES

[1] S. N. Bland, Y. E. Krasik, D. Yanuka, R. Gardner, J. Macdonald, A. Virozub, S. Efimov, S. Gleizer, and N. Chaturvedi, Phys. Plasmas **24**, 082702 (2017).

[2] D. Yanuka, S. Theocharous, and S. N. Bland, Phys. Plasmas **26**, 122704 (2019).

[3] Y. E. Krasik, S. Efimov, D. Sheftman, A. Fedotov-Gefen, O. Antonov, D. Shafer, D. Yanuka, M. Nitishinskiy, M. Kozlov, L. Gilburd, G. Toker, S. Gleizer, E. Zvulun, V. T. Gurovich, D. Varentsov, and M. Rodionova, IEEE Trans. Plasma Sci. **44**, 412 (2016).

[4] D. Shafer, V. T. Gurovich, D. Yanuka, E. Zvulun, S. Gleizer, G. Toker, and Y. E. Krasik, J. Appl. Phys. **117**, 015901 (2015).

[5] D. Maler, S. Efimov, A. Rososhek, S. N. Bland, and Y. E. Krasik, Phys. Plasmas **28**, 063509 (2021).

[6] D. Maler, M. Kozlov, S. Efimov, and Y. E. Krasik, Phys. Plasmas **29**, 032705 (2022).

[7] D. Maler, R. Grikshtas, S. Efimov, L. Merzlikin, M. Liverts, M. Kozlov, and Y. E. Krasik, Phys. Plasmas **30**, 022710 (2023).

[8] S. Lyon and J. Johnson, *Sesame: The Los Alamos National Laboratory Equation of State Database*, Report No. LA-UR-92-3407 (Los Alamos National Laboratory, 1992).

[9] M. P. Olbinado, X. Just, J.-L. Gelet, P. Lhuissier, M. Scheel, P. Vagovic, T. Sato, R. Graceffa, J. Schulz, A. Mancuso, J. Morse, and A. Rack, Opt. Express **25**, 13857 (2017).

[10] S. P. Theocharous, S. N. Bland, D. Yanuka, A. Rososhek, M. P. Olbinado, A. Rack, and Y. E. Krasik, Rev. Sci. Instrum. **90**, 013504 (2019).

[11] P. Cloetens, R. Barrett, J. Baruchel, J.-P. Guigay, and M. Schlenker, J. Phys. D: Appl. Phys. **29**, 133 (1996).

[12] D. Yanuka, A. Rososhek, S. Theocharous, S. N. Bland, Y. E. Krasik, M. P. Olbinado, and A. Rack, J. Appl. Phys. **124**, 153301 (2018).

[13] D. Yanuka, A. Rososhek, S. Theocharous, S. N. Bland, Y. E. Krasik, M. P. Olbinado, A. Rack, and E. V. Oreshkin, Phys. Plasmas **26**, 050703 (2019).

[14] D. Maler, S. Efimov, M. Liverts, S. Theocharous, J. Strucka, Y. Yao, W. Proud, A. Rack, B. Lukic, S. N. Bland, and Y. E. Krasik, Phys. Plasmas **29**, 063502 (2022).

[15] J. Strucka, B. Lukic, M. Koerner, J. W. D. Halliday, Y. Yao, K. Mughal, D. Maler, S. Efimov, J. Skidmore, A. Rack, Y. Krasik, J. Chittenden, and S. N. Bland, Phys. Fluids **35**, 044108 (2023).

[16] A. Rososhek, S. Efimov, A. Virozub, D. Maler, and Y. E. Krasik, Appl. Phys. Lett. **115**, 074101 (2019).

[17] M. P. Olbinado, V. Cantelli, O. Mathon, S. Pascarelli, J. Grenzer, A. Pelka, M. Roedel, I. Prencipe, A. L. Garcia, U. Helbig, D. Kraus, U. Schramm, T. Cowan, M. Scheel, P. Pradel, T. De Resseguier, and A. Rack, J. Phys. D: Appl. Phys. **51**, 055601 (2018).

[18] A. Grinenko, A. Sayapin, V. T. Gurovich, S. Efimov, J. Felsteiner, and Y. E. Krasik, J. Appl. Phys. **97**, 023303 (2005).

[19] A. Sayapin, A. Grinenko, S. Efimov, and Y. E. Krasik, Shock Waves **15**, 73 (2006).

[20] A. Fedotov, A. Grinenko, S. Efimov, and Y. E. Krasik, Appl. Phys. Lett. **90**, 201502 (2007).

[21] M. S. Del Rio and L. Rebuffi, AIP Conf. Proc. **2054**, 060081 (2019).

[22] M. C. Leu, P. Meng, E. S. Geskin, and L. Tismeneskiy, J. Manuf. Sci. Eng. **120**, 571 (1998).

[23] A. Guha, R. M. Barron, and R. Balachandar, J. Mater. Process. Technol. **211**, 610 (2011).

[24] V. Gurovich, A. Virozub, A. Rososhek, S. Bland, R. B. Spielman, and Y. E. Krasik, J. Appl. Phys. **123**, 185902 (2018).

[25] J. R. MacDonald, Rev. Mod. Phys. **38**, 669 (1966).

[26] R. H. Cole, *Underwater Explosions* (Princeton University Press, Princeton, NJ, 1948).

[27] Y. B. Zel'dovich and Y. P. Raizer, *Physics of Shock Waves and High-Temperature Hydrodynamic Phenomena*, 1st ed. (Academic Press, 1966).

[28] G. Bazalitski, V. T. Gurovich, A. Fedotov-Gefen, S. Efimov, and Y. E. Krasik, Shock Waves **21**, 321 (2011).

[29] See https://www.ansys.com/products/structures/ansys-ls-dyna for additional information about the simulation.

[30] LS-DYNA®, Dev, LS-DYNA (Livermore Software Technology (LST), 1992), pp. 22-40–22-43.

[31] G. Mie, Ann. Phys. **316**, 657 (1903).

[32] E. Grüneisen, Ann. Phys. **344**, 257 (1912).

[33] M. K. Mohd Nor, C. S. Ho, N. Ma'at, and M. F. Kamarulzaman, Contin. Mech. Thermodyn. **32**, 1217 (2020).

[34] M. Otsuka, Y. Matsui, K. Murata, Y. Kato, and S. Itoh, *8th International LS-DYNA Users Conference* (Livermore Software Technology Corporation, Livermore, CA, 2004), p. 5.

17 April 2024 11:07:44